CHAPTER – 2

Literature Review

2.1 Introduction to biomaterials

A biomaterial is a non-viable substance used in medical applications, and it should not have any toxic or harmful effects on the physiological environment, ensuring harmonious coexistence with the surrounding tissue [9-10]. Additionally, a biomaterial must possess sufficient biocompatibility for its desired application. Individuals with degenerative joint problems or those who have experienced accidents often require surgery to replace damaged joints or repair fractured bones with suitable implants [10]. These implants are biomaterials inserted into the body for a substantial period to replace, support, or enhance the function of damaged tissues, organs, or structures [11]. In modern times, increased population has probabilistically made more human beings accident prone, resulting in significantly higher demand for implants.

Over the past few decades, metallic biomaterials have been extensively utilized in implants and surgical equipment because of their exceptional attributes, such as superior strength and toughness, excellent wear and corrosion resistance, as well as good biocompatibility [8,12]. Generally, the service life of these implant biomaterials ranges from 15 to 20 years. In some cases, patients undergo MRI scans after implantation to evaluate the positioning and condition of the implant. To facilitate this, the implants are designed to be MRI-compatible, ensuring they exhibit low magnetic susceptibility [13].

2.2 Various modes of failure of orthopedic implant materials

2.2.1 Improper loading of the implant

The service conditions of implants are highly complex, as both static and dynamic loads are operative according to the patient's activities. The amount of load varies across different body parts; for instance, the hip, knee, and femur experience loads that are roughly four, three, and two times the body weight, respectively [14-15]. Temporary implants are used to hold the fractured ends of bones together, promoting healing and joining [16]. During this process, both bones and implants share the load. However, if the implants lack sufficient strength, they may fail due to localized plastic deformation caused by overloading and excessive stress [14,17].

In addition to this, implants may also fail due to loosening, which can lead to bone resorption (a reduction in bone mineral density). This occurs when, after surgery, the implants exhibit significantly higher elastic modulus compared to the surrounding bone [18-20]. As a result, the load or stress is not uniformly distributed between the bone and the implants, causing the implants to bear nearly the entire applied load while bypassing the bone in physiological environments. This phenomenon is known as the stress shielding effect, and its mechanism is schematically represented in Figure 2.1.

In Figure 2.1 (a), the elastic modulus of the implant is similar to that of natural bone. When stress (from body weight) is applied to the top of the femur, it is uniformly distributed through the trabeculae in the femoral head and then transmitted through the cortical bone. However, if the elastic modulus of the implant is significantly higher compared to the bone, stress is transferred down the implant stem, bypassing the bone. As a result, the bone near the implant (highlighted in the circled area in Figure 2.1 (b)) experiences reduced stress, which causes bone loss. Over time, this lack of load weakens the bone, making it thinner and less dense. This can ultimately lead to implant loosening (as shown in Figure 2.1 (c)), fractures, or further surgeries required.

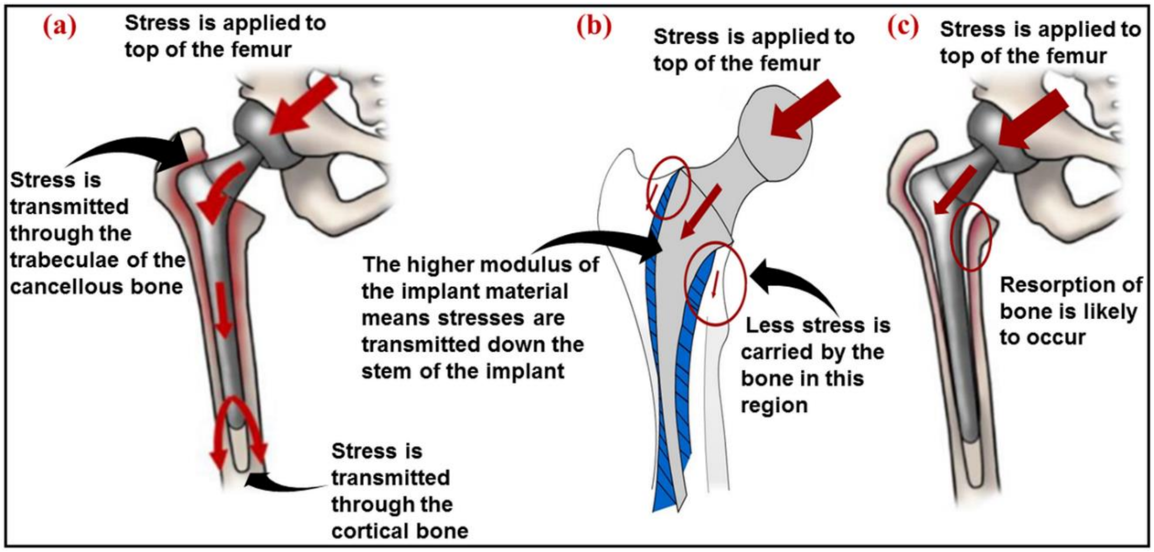

Figure 2.1 Schematic representation of the stress shielding mechanism caused by the non-uniform distribution of load between the implant and the bone (adapted from [20]).

2.2.2 Corrosion of implants

In biomedical engineering and healthcare, corrosion-induced implant failure is a serious concern since it could affect performance, biocompatibility, and durability [21]. Implants in the human body are subjected to a challenging atmosphere that includes exposure to blood, water, sodium, chlorine, and proteins. The human physiological environment contains a 0.9% saline solution with a pH of ~7.4. However, due to biological changes caused by infections and diseases, the pH of the physiological solution can fluctuate between 3 and 9, which significantly affects the corrosion of implants [22]. In general, the common types of corrosion that can affect implants include pitting, stress corrosion cracking, crevice corrosion, and fretting corrosion.

2.2.3 Friction and wear of implants

Friction and wear are among the most critical issues causing the failure of many medical devices, particularly orthopedic and dental implants [22-23]. Under physiological conditions, the application of load causes implants to degrade over time. As a result, small particles (wear debris) are generated, which influence inflammatory responses, leading to osteolysis and loosening of the implant [24]. The failure of implants due to loosening is a serious concern, as 75% of joint replacements fail as a result of aseptic loosening [25]. Also, the release of metallic ions due to wear and friction may cause toxic or allergic reactions in the surrounding tissues. Consequently, this significantly affects the cytocompatibility of the implant.

2.3 Metallic implant biomaterials

Several metallic materials are widely used as implant biomaterials, including 316L stainless steel (SS), Co-Cr-based alloys, Ti and Ti-based alloys, Ni-Ti shape memory alloys, Mg alloys, Ta and Ta-based alloys, as well as gold and silver [9]. These materials were extensively utilized in biomedical applications due to their superior mechanical and electrochemical properties in physiological environments. Figure 2.2 schematically illustrates the application of various conventional metals and alloys in the biomedical field [26-27]. The mechanical properties of some of these metallic biomaterials and cortical bone are shown in Table 2.1.

Table 2.1 Mechanical properties of metallic biomaterials and cortical bone [9-10,28-29].

Metallic biomaterials	**Elastic modulus**	**Ultimate tensile**	**Total elongation**	**Fracture toughness**
316L SS	200	540-1000	45	~100
CoCrMo	240	900-1540	8	~100
Ti alloys	105-125	900	12	~80
Mg alloys	40-45	100-250	6-8	15-40

Ni-Ti alloy	30-50	1355	25	30-60
Cortical bone	10-30	130-150	1.5	2-12

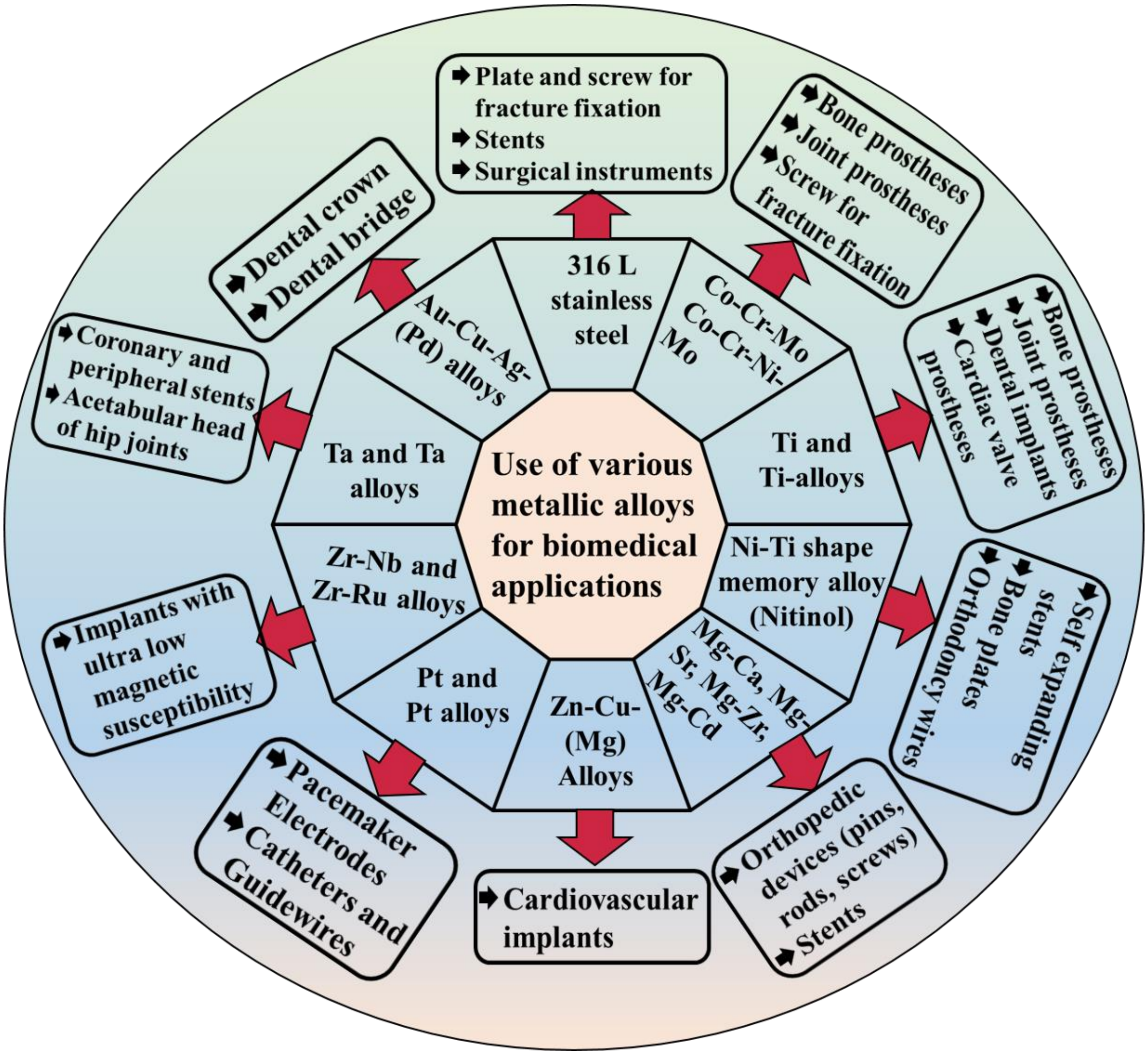

Figure 2.2 Schematic representation of various conventional metals and alloys commonly used in biomedical applications (adapted from [26-27]).

However, apart from the aforementioned properties, conventional metallic biomaterials have some critical issues that limit their long-term clinical applications. The conventional metallic biomaterials release toxic metallic ions, such as Co, Ni, V, Al, and Cr, in the physiological environment. The release of Co from the implants due to corrosion and wear significantly damages the tissue in the vicinity of the prostheses [30]. Additionally, Co can cause painful dyspnea (difficulty breathing), DNA damage, memory problems, severe headaches, and potential promotion of tumors. There is also a risk of Co poisoning and neurological issues [31-32]. Similar to Co, Ni release also exhibits toxicity and carcinogenicity. Notably, Ni ions are associated with causing skin-related diseases, respiratory disorders, lung cancer, tissue irritation, as well as liver and kidney damage [33-34].

Vanadium also negatively impacts cellular responses in the physiological environment. Its effects include carcinogenicity and several adverse impacts on bone softening, respiratory system, liver, blood parameters, and the neurological system [35]. Aluminum is also a neurotoxic element at high doses, contributing to various other diseases. These include brain neurotoxicity (such as Alzheimer’s disease), kidney damage, contact dermatitis, and an increased risk of blood cancer [36-37]. Apart from these, chromium (Cr) exhibits both positive and negative cellular responses. A deficiency of Cr can lead to hyperglycemia (elevated blood sugar) and glycosuria (presence of glucose in urine), while an excess of Cr can cause various other diseases. These include skin-related disease, liver and kidney failure, as well as an increased risk of cancer [38-39].

Additionally, the elastic modulus of most conventional metallic biomaterials is significantly higher than that of cortical bone, as shown in Table 2.1. This higher elastic modulus results in a non-uniform distribution of load between the implant and the bone. Consequently, bone loss and implant loosening occur due to the movement of the implant, which opposes bonding to the bone. This leads to implant failure, necessitating revision surgery [9]. To address the aforementioned challenges, researchers have often sought to improve or modify the existing conventional metallic biomaterials, or search for new alternatives. Recently, high-entropy alloys (HEAs) and the broader category of complex concentrated alloys (CCAs) have opened up new possibilities for designing a wide range of innovative alloys, presenting an alternate pathway to traditional metallic biomaterials [40-42].

2.4 High entropy alloys

High-entropy alloys are multicomponent systems containing five or more principal elements, with their atomic concentrations ranging between 5 to 35% [3,43]. Additionally, the configurational entropy (ΔS_{mix}) of these alloys is greater than 1.5 R, where R represents the gas constant [43]. Boltzmann's equation is used to calculate the configurational entropy of an alloy system as follows:

$$\Delta S_{\mathrm{mix}} = \mathrm{k} \ln \mathrm{w} \text{ .... (2.1)}$$

where, k and w are Boltzmann's constant and various number of ways of arranging the atoms at the atomic sites, respectively. Therefore, the ΔS_{mix} for the formation of solid solution for n element system with X_i mole fraction is given as:

$$\Delta S_{\mathrm{mix}} = -\mathrm{R} \sum_{\mathrm{i}=1}^{\mathrm{n}} \mathrm{X_i} \ln \mathrm{X_i} \text{ .... (2.2)}$$

Many alloy systems are also classified based on their calculated configurational entropy. Alloys with a ΔS_{mix} value less than 1 R are categorized as low-entropy or conventional alloys. If the ΔS_{mix} value is between 1 R and 1.5 R, they are classified as medium-entropy alloys (MEAs). Finally, alloys with a ΔS_{mix} value greater than 1.5 R are categorized as HEAs [43]. Figure 2.3 shows the relationship between configurational entropy and the number of elements in an equimolar alloy. It is observed that as the number of elements increases, initially configurational entropy increases rapidly. However, beyond a certain point (up to number of elements 13), adding more elements increases the complexity of alloy synthesis, making it more challenging, while the configurational entropy only shows a gradual increase [43].

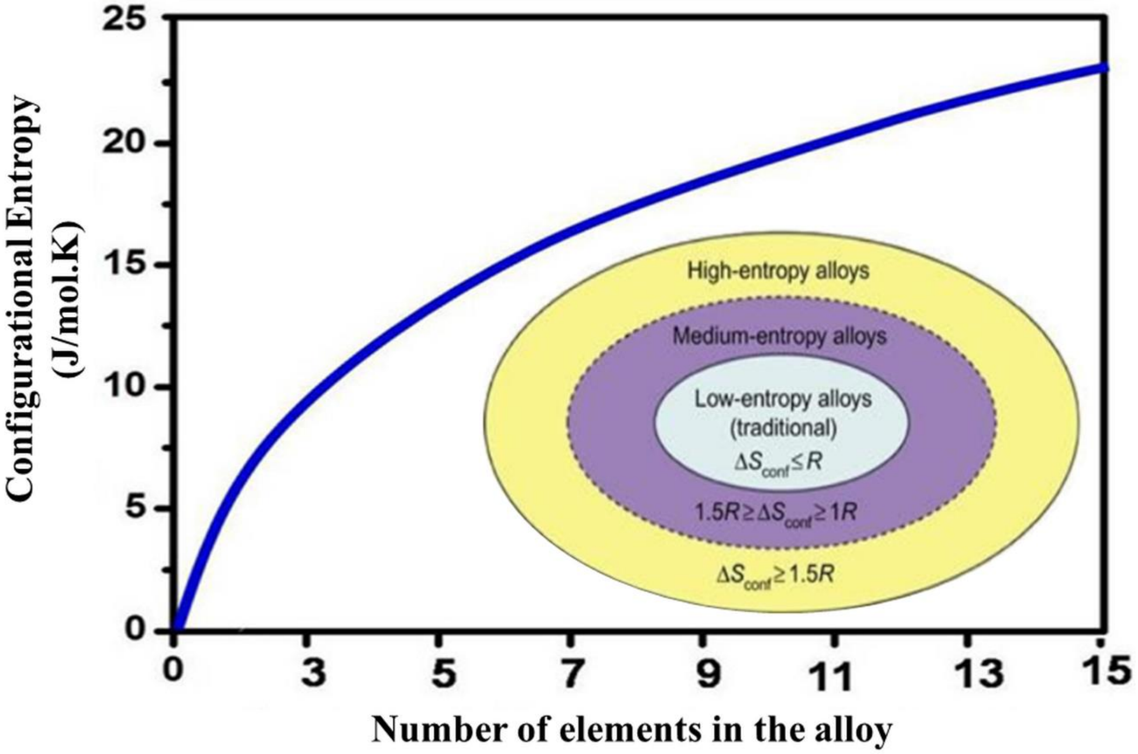

Figure 2.3 The variation of configurational entropy (ΔS_{mix}) for an equimolar alloy with a number of elements (adapted from [43]).

As discussed above, based on the composition and entropy-based definition, HEAs were originally closely associated with the formation of single-phase solid solutions through the control of configurational entropy. Later on, the development of non-equiatomic HEAs, multi-phase HEAs, HEAs with interstitial alloying elements, MEAs, and other variations led to the broader family of CCAs [5,44]. The compositional space for equiatomic HEA is extremely constrained. In a compositional hyperspace, as shown in Figure 2.4, equiatomic HEAs occupy the central region, while CCAs surround them, significantly expanding the overall compositional space. This expanded compositional space provides increased flexibility and diversity in selecting constituent alloying elements and adjusting their stoichiometric ratios to achieve the desired CCA compositions.

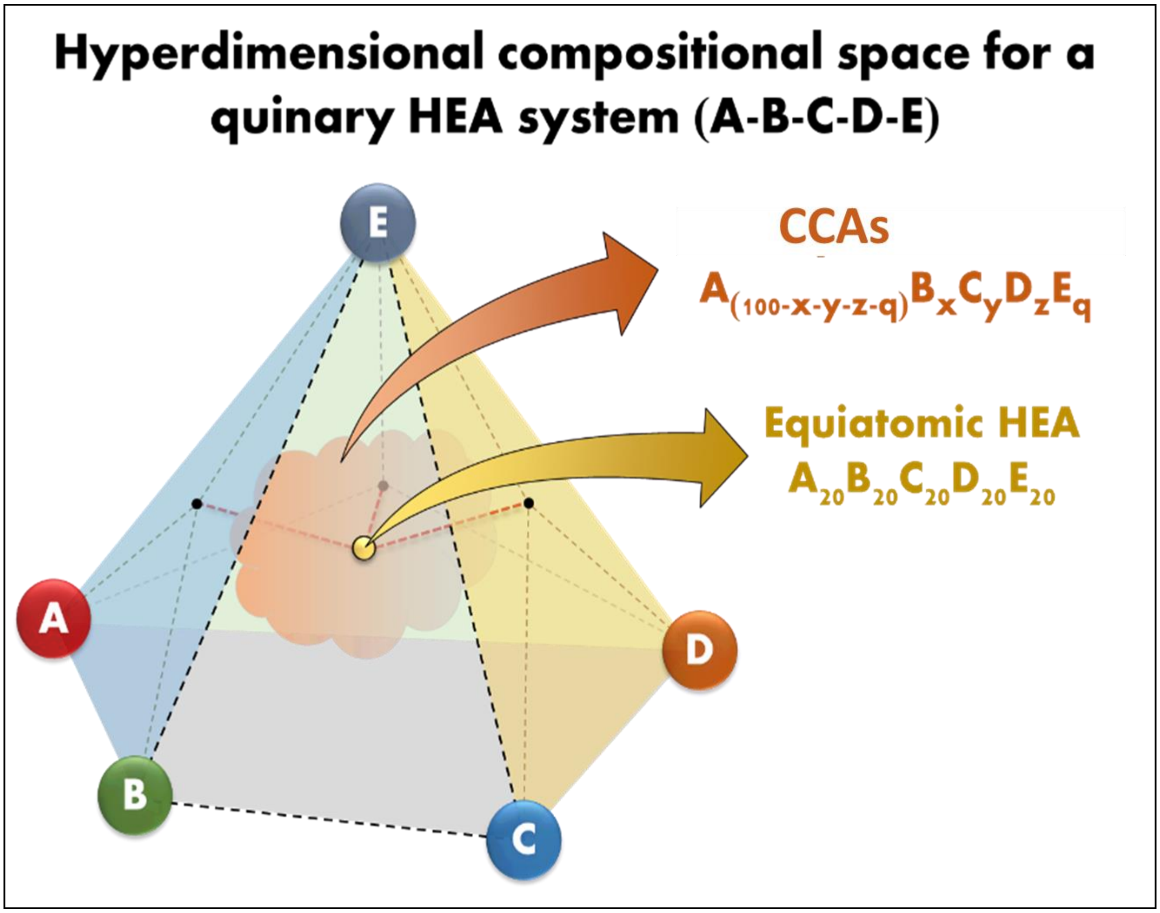

Figure 2.4 Schematic representation of evolution in the compositional domains of equiatomic HEA and CCAs in a hyper-dimensional compositional space.

2.5 Core effects of high entropy alloys

The microstructure and properties of HEAs are influenced by several factors, among which four core effects are considered the most fundamental. Figure 2.5 shows the schematic representation of the core effects of high entropy alloys, including high entropy effect, severe lattice distortion, sluggish diffusion, and cocktail effect. In terms of thermodynamics, the high-entropy effect may hinder the formation of complex phases. Regarding kinetics, the sluggish diffusion effect can retard the phase transformation. In terms of structure, severe lattice distortion can significantly change the properties. As for properties, a cocktail effect results in values that exceed those predicted by the mixture rule, due to the mutual interactions of dissimilar atoms and intense lattice distortion.

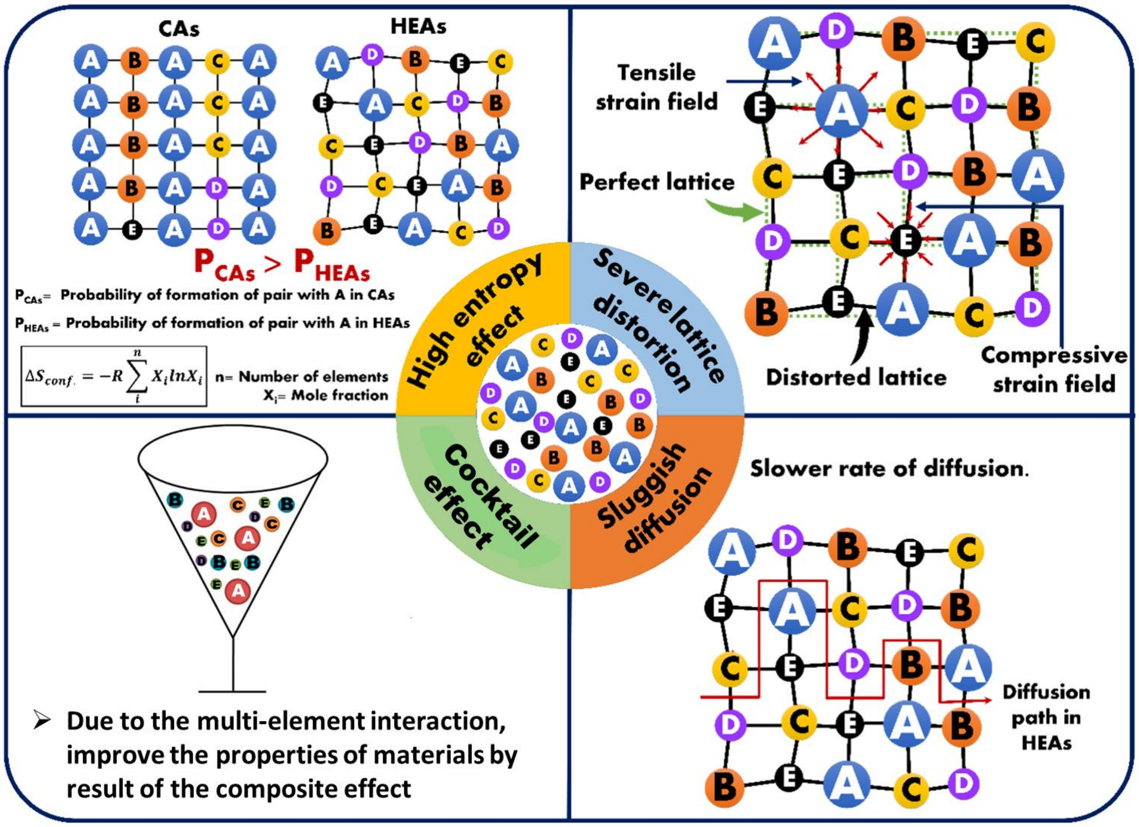

Figure 2.5 Schematic representation of core effects of high entropy alloys.

2.5.1 High entropy effect

The High-Entropy Effect, a prominent characteristic of HEAs, suggests that increased configurational entropy promotes the formation of solid solution phases over competing intermetallic compounds. According to principles of physical metallurgy, it can be anticipated that these alloys will develop a multiphase structure containing intermetallic compounds, when the influence of configurational entropy was neglected. Unlike traditional metallurgy principles, the high configurational entropy of HEAs reduces the free energy of solid solution phases. This, in turn, enhances mutual solubility among the constituent elements, thereby decreasing the number of phases formed. According to the Gibbs free energy equation, $\Delta \mathrm{G}_{\mathrm{mix}} = \Delta \mathrm{H}_{\mathrm{mix}} - \mathrm{T}\Delta S_{\mathrm{mix}}$ (where $\Delta \mathrm{G}_{\mathrm{mix}}$ represents the Gibbs free energy of mixing, $\Delta \mathrm{H}_{\mathrm{mix}}$ is the mixing enthalpy, and T is the temperature), it can be inferred that a higher ΔS_{mix} significantly reduces $\Delta \mathrm{G}_{\mathrm{mix}}$ [45]. Consequently, the lower free energy of mixing in HEAs enhances the stability of the solid solution phase.

2.5.2 Severe lattice distortion effect

In the HEAs, unlike in traditional alloys, each atom is surrounded by a variety of different atoms. These atoms differ in their electronic configurations, sizes, and bonding characteristics, leading to displacements within the lattice. As a result, the average lattice distortion in HEAs is significantly more pronounced than in conventional alloys. Figure 2.5 shows the schematic representation of a strained lattice in HEAs. The high configurational entropy is also associated with the severe distortion, as this distortion increases the uncertainty in atomic positions, thereby increasing the configurational entropy. Consequently, this leads to a decrease in the X-ray diffraction peak intensity due to diffuse scattering [46-47].

In addition to this, the lattice distortion effect significantly influences the properties, including hardness, strength, and electrical and thermal conductivity of the HEAs. The strength and hardness of the HEAs are significantly enhanced due to solid solution hardening, which arises from the heavily distorted lattice structure. The local tensile and compressive strain fields are generated within the lattice due to the presence of smaller atoms near larger ones and larger atoms near smaller ones, ensuring lattice integrity as illustrated in Figure 2.5. These localized lattice strain fields interact with the strain fields of dislocations, hindering their movement strengthening the material. Also, the severe lattice distortion may influence the scattering of electrons and phonons during propagation, impacting the electrical and thermal conductivity [47].

2.5.3 Sluggish Diffusion Effect

The diffusion kinetics in HEAs is significantly slower compared to conventional alloys due to the presence of various types of atoms. The mechanism of slow diffusion is also illustrated in Figure 2.5. The schematic shows that in HEAs, atom A is surrounded by a variety of different atoms. This leads to greater variations in lattice potential energy (LPE), which affects the activation energy for diffusion by impeding atomic movement. Tsai et al. used the seven-bond model to study the impact of local potential energy fluctuations on diffusion in CoCrFeMnNi HEAs [48]. Their findings revealed that the local potential energy for Ni diffusion in Co-Cr-Fe-Mn-Ni alloys is 50% higher than that in ternary Fe-Cr-Ni alloys, as shown in Figure 2.6 (b), demonstrating that diffusion in HEAs is remarkably sluggish.

Additionally, Figure 2.6 (a) illustrates the melting-point-normalized activation energy (Q/T_m) for the diffusion of Ni, Co, Fe, Mn, and Cr in various metals and alloys. The Figure indicates that the Q/T_m for HEAs is higher compared to pure metals and stainless steel, suggesting that the greater the number of elements with varying atomic sizes, slower the diffusion rate [1,48]. This sluggish diffusion effect impedes the atomic movement and phase transformation, resulting in enhanced creep resistance, a reduced coarsening rate, creation of fine precipitates, elevated recrystallization temperatures, and diminished creep growth.

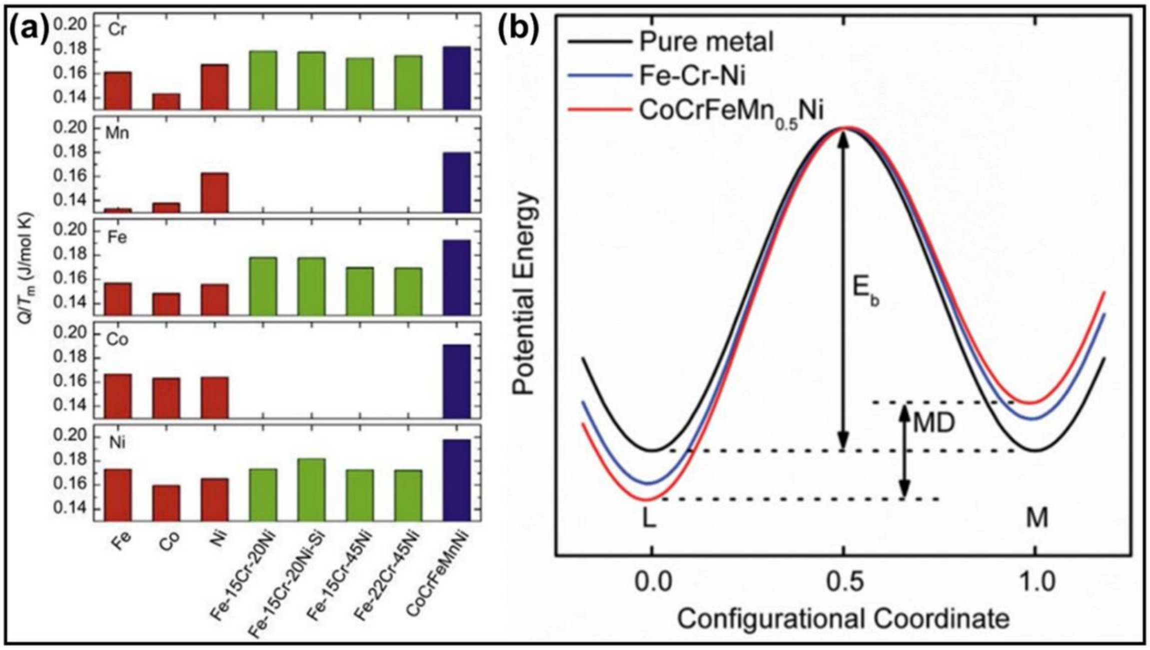

Figure 2.6 (a) Comparison of activation energy of diffusion normalized with melting point for Ni, Co, Fe, Mn, and Cr in various metals and alloys, and (b) schematic representation of potential energy change during diffusion of Ni in pure metal and alloys [1,48].

2.5.4 Cocktail effect

In HEAs, a unique cocktail effect accounts for enhanced properties due to the presence of at least five principal elements [49]. HEAs can consist of one, two, or multiple phases, depending on their composition and processing methods. The overall properties result from the contributions of all the phases, influenced by factors such as crystal structure, size, shape, distribution, phase boundaries, and the properties of each phase. Also, each phase is a multicomponent solid solution, which can be considered an atomic-scale composite. The composite characteristics arise not only from the elemental properties according to the mixture rule but also from the interactions between elements and the significant lattice distortions. These interactions and distortions lead to additional contributions over and above what the mixture rule would have predicted. The "cocktail effect" encompasses atomic-scale multicomponent composites to microscale multiphase composite effects.

2.6 Design of HEAs/CCAs

The desire to investigate the central compositional region of the phase diagrams and the surprisingly stabilizing simple solid solution phases in the microstructure was the primary motivation behind the development of equiatomic HEAs. Over nearly two decades, the field of HEAs has experienced a significant evolution in design strategies. Additionally, the fundamental principles behind the design of CCAs, which may appear unclear, actually arise from the combination of traditional metallurgical design concepts used for conventional alloys with the HEA design approach. This was actually required, as it expands the compositional range provided by HEAs, enabling the creation of alloys with unique compositions necessary to form traditional microstructures or morphologies (such as a eutectic composition that encourages the formation of a dual-phase microstructure, as seen in conventional eutectic alloys), which may not be achievable with the equiatomic compositions found in HEAs alone.

As the HEA field advanced, it saw the adoption of a wide range of tools and methods for designing new HEAs, followed by experimental validation. These approaches include the use of high-throughput calculations, density functional theory (DFT), and calculation of phase diagram (CALPHAD) for thermodynamic modelling [50–51]. However, it was noted that techniques such as DFT calculations are time-consuming and show uncertainties when it comes to handling the d-orbitals of transition-metal atoms, which are commonly found in HEAs [52]. Perhaps the most widespread method has been the CALPHAD approach. This method relies on creating phase diagrams based on the data in these databases, and applying computational techniques for calculating thermodynamic properties related to phase coexistence and stability [53]. Specifically, the CALPHAD approach can be utilized to assess relative phase stabilities, individual component solubilities, transition temperatures, and phase fractions.

2.6.1 Empirical model for predicting phase stability and phase evolution

According to the classic Hume-Rothery rules, the formation of binary solid solutions is influenced by factors such as differences in atomic size, crystal structure, valency, and electronegativity [54]. In addition to these parameters, the mixing enthalpy (ΔH_{mix}) and configurational entropy are key parameters that play a crucial role in phase formation for HEAs. Among these parameters, the role of configurational entropy (ΔS_{mix}) was already discussed in section 2.4. The remaining parameters can be defined as follows:

The atomic size difference (δ) of these alloys for 'n' number of elements is calculated as:

$$\delta = \sqrt{\sum_{i=1}^{n} c_i \left(1 - \frac{r_i}{\bar{r}}\right)^2} \;\ldots\ldots\ldots\ldots\ldots\ldots.. \text{(2.3)}$$

where c_i and r_i are the atomic concentration and atomic radius of the i^{th} element, respectively, and $\bar{r}$ is the average atomic radius. The mixing enthalpy is utilized to evaluate the chemical compatibility of the alloying elements in HEAs. For a solid solution, its value is calculated using the following equation:

$$\Delta H_{mix} = 4 \sum_{i=1, i \neq j}^{n} \Delta H_{ij}^{mix} c_i c_j \;\ldots\ldots\ldots\ldots\ldots \text{(2.4)}$$

where ΔH_{ij}^{mix} represents the mixing enthalpy of a binary equiatomic alloy, estimated using Miedema's semi-empirical model.

Zhang et al. [55] and Guo et al. [56] investigated the influence of the aforementioned parameters on the formation of solid solution phases in HEAs. They suggested that solid solution phases (ordered/disordered) are likely to form when ΔS_{mix}, δ, and ΔH_{mix} lie within the ranges of $11 \leq \Delta S_{mix} \leq 19.5$ J/(K mol), $0 \leq \delta \leq 8.5$, and $-22 \leq \Delta H_{mix} \leq 7$ KJ/mol, respectively. Furthermore, when these parameters specifically lie within the ranges $12 \leq \Delta S_{mix} \leq 17.5$ J/(K mol), $\delta \leq 4.3$, and $-15 \leq \Delta H_{mix} \leq 5$ KJ/mol, simple disordered solid solution phases are predominantly formed [45]. In addition to these parameters, another thermodynamic parameter Ω was used to predict the phase formation criteria in HEAs. This parameter is based on the competition between enthalpy and entropy, providing further insight into the stabilization of different phases [57].

$$\Omega = \frac{T_m \Delta S_{mix}}{|\Delta H_{mix}|} \ldots\ldots\ldots\ldots\ldots\ldots\ldots\ldots (2.5)$$

Ω indicates the influence of entropy in comparison to enthalpy. Therefore, a larger Ω implies a greater probability of forming a disordered solid solution phase, which is consistent with the analysis. In line with the values of the previously mentioned thermo-physical parameters, the various phases observed in high-entropy materials are schematically illustrated in Figure 2.7.

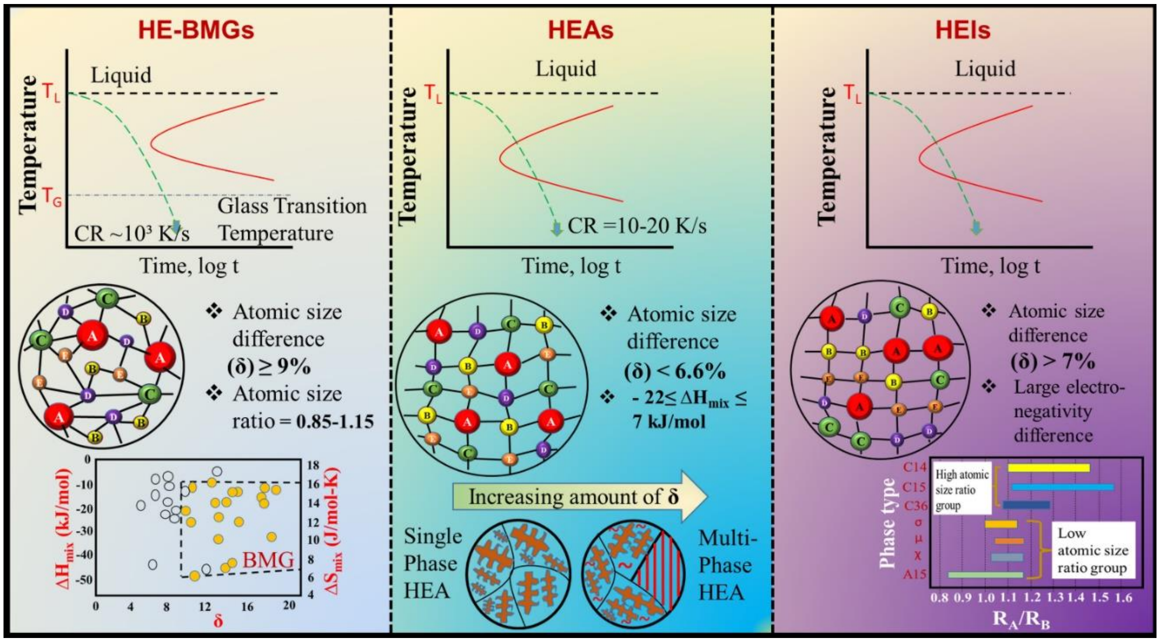

Figure 2.7 Schematic representation of the distinct phases observed in various high entropy materials (HE-BMGs, HEAs, and high entropy intermetallics (HEI)).

The valence electron concentration (VEC) of these alloys provides a general understanding of their simple structures [58]. It serves as a crucial factor in predicting the formation of BCC and FCC phases in HEAs. The VEC of an alloy can be calculated using the following equation:

$$\mathrm{VEC} = \sum_{i=1}^{n} c_i (\mathrm{VEC})_i \text{ .... } (2.6)$$

where, $(\mathrm{VEC})_i$ is the VEC for ith elements. An alloy will stabilize in an FCC structure if its VEC is ≥ 8 and in a BCC structure if the VEC is ≤ 6.87. However, both structures (BCC + FCC) can coexist within the intermediate range.

2.6.2 Design of bio-CCAs

CCAs designed for biomedical applications typically exhibit high hardness and strength, contributing to their exceptional friction and wear resistance, as well as excellent corrosion resistance. Also, bio-CCAs should be composed of constituent elements that ensure strong biocompatibility, incorporating non-toxic and non-allergenic behaviour. The selection of constituent elements is particularly critical for bio-HEAs/CCAs. Commonly, elements suitable for biomedical use include Ti, Mg, Cu, Zn, Zr, Hf, Cr, Nb, Mo, Ta, W, Ag, and Sn, as the release of these elements in the physiological environment remains within a safe range of biological effects throughout their entire service life [59]. Figure 2.8 schematically represents the taxonomy of constituent elements, design attributes, and phases in bio-CCAs.

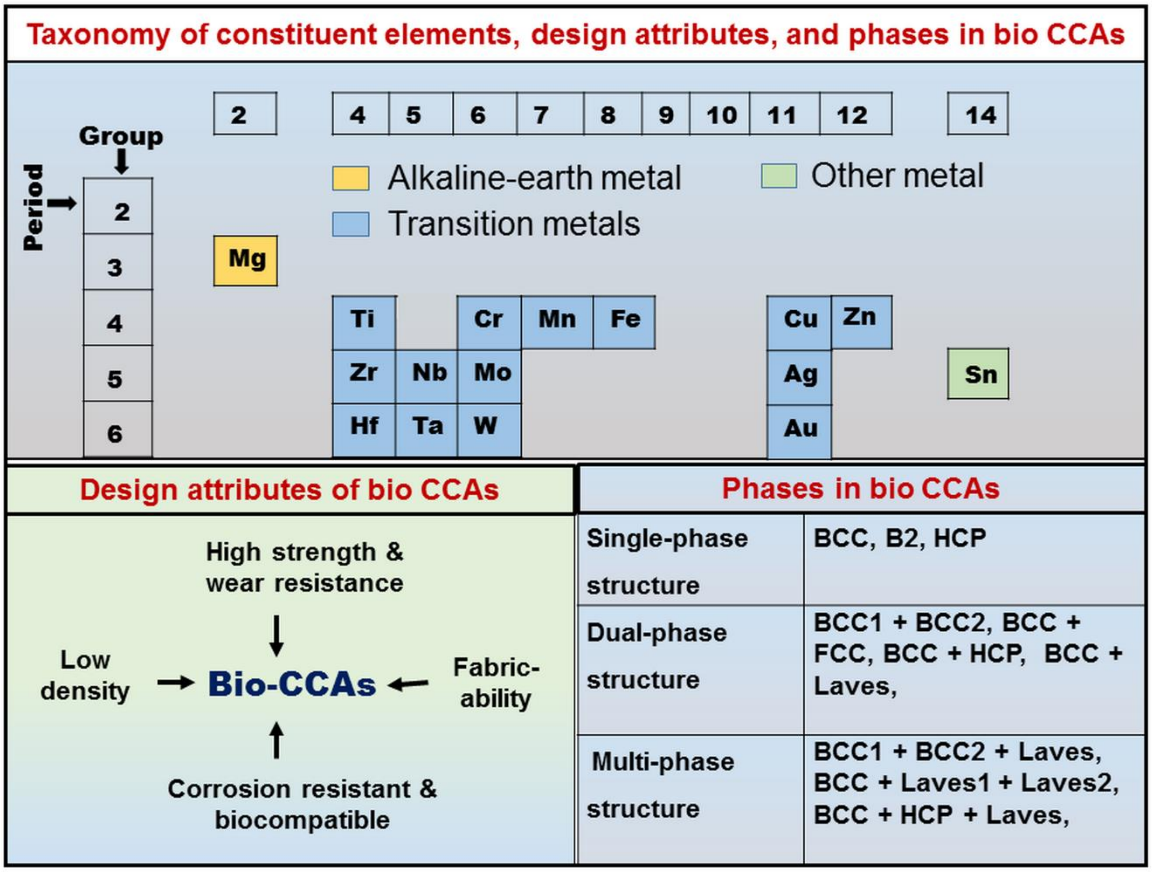

Figure 2.8 Taxonomy of constituent elements, design attributes, and phases in bio-CCAs, BCC: body centered cubic, FCC: face centered cubic, HCP: hexagonal closed packed, B2: ordered BCC structure.

2.7 Synthesis and processing routes for bio-CCAs

HEAs/CCAs are synthesized using various processing methods, including solid-state processing (such as mechanical alloying), melting and casting techniques (like vacuum arc or vacuum induction melting), and solid deposition methods. Among these processing methods, the melting and casting route is the most commonly used for synthesizing bio-HEAs/CCAs. Several bio-HEAs were created through vacuum arc melting, which utilizes an electric arc to melt various metals at high temperatures [34,59-61]. A schematic representation of the vacuum arc melting process, along with its corresponding steps, is illustrated in Figure 2.9. In this technique, alloy metal pieces with appropriate compositions are placed on a water-cooled copper crucible. A high vacuum is created, followed by the introduction of Ar gas into the melting chamber. Then, high-voltage power is supplied, generating an arc between a non-consumable tungsten electrode and the copper hearth. Subsequently, the metal pieces are melted and solidified in the copper mold. Quite a few biocompatible HEAs/CCAs were developed using vacuum arc melting technique so far, e.g., equimolar and non-equimolar in Ti-Zr-Nb-Hf [62], Ti-Zr-Nb-Hf-Ta-Mo [63], Ti-Zr-Hf-Nb-Mo [64], Ti-Zr-Nb-Ta-Mo [40], Ti-Zr-Hf-Nb-Ta [34,65], Ti-Zr-Nb-Ta-Fe [66], Ti-Zr-Hf-Nb-Fe [67], Ti–Zr-Hf-Cr-Mo [68], and Ti-Mo-Nb-Ta-W-Cr [69].

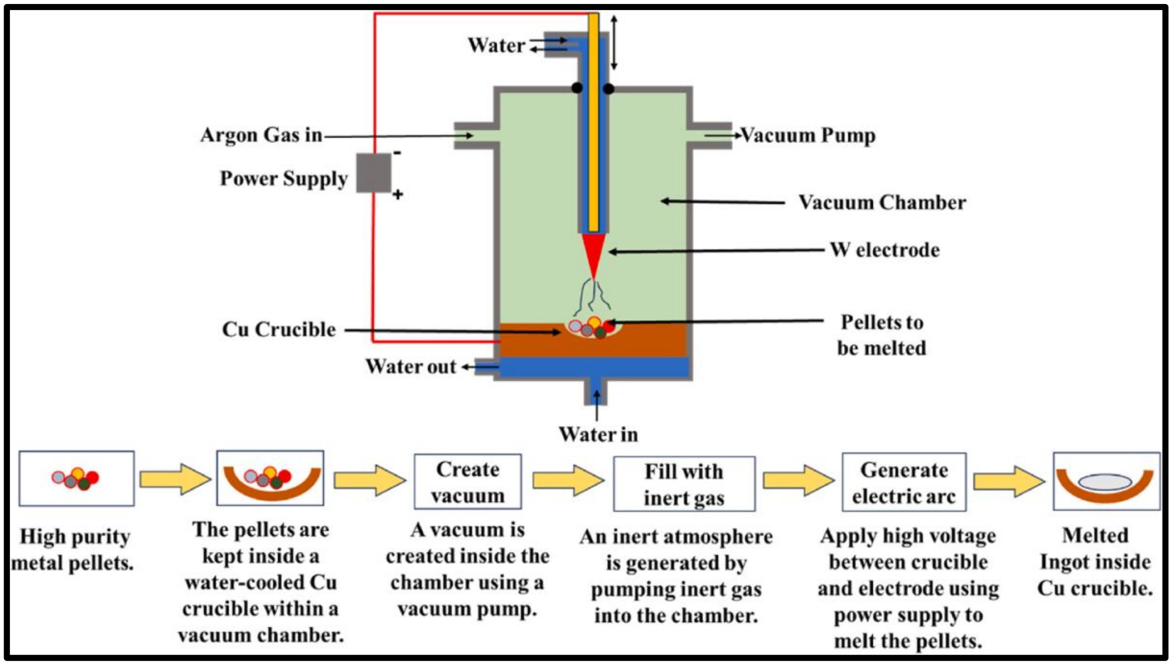

Figure 2.9 Schematic representation of the vacuum arc melting process [59].

Many studies have reported that HEAs are developed using casting techniques, which often result in issues such as composition segregation, shrinkage cavities, and high internal stress [57,70]. These casting defects are challenging to avoid; however, effective postprocessing techniques can minimize these defects, consequently enhancing the properties of HEAs. One of the most effective techniques to address these defects is hot rolling. It is an efficient technique for converting cast structures into wrought structures, as it refines the grain structure and improves mechanical properties [71]. However, this process has certain drawbacks, such as the formation of edge cracks. These cracks are removed through machining, but machining increases the overall manufacturing costs. An alternative effective method is heat treatment, which homogenizes the material, promotes phase homogeneity, and reduces internal stresses in the alloy [69,72]. Several research studies have shown that heat treatment (annealing treatment) significantly reduces casting defects, resulting in improved properties of alloys including AlCrFeMnNi [73], TiZrNbMoTa [40], and TiZrNbTa [74].

In addition, high-pressure torsion (HPT) is an effective processing technique for reducing the elemental segregation of the as-cast HEAs. It is a severe plastic deformation (SPD) technique that creates ultrafine grains and induces lattice defects, such as dislocations and vacancies [75-77]. As a result, the elastic modulus of the alloys decreases, reducing the elastic modulus mismatch between the bone and metallic implants, which, in turn, reduces the stress shielding effects. The HPT processed biocompatible CCAs reported so far include TiAlFeCoNi [75], Ti-Nb-Zr-Ta-Fe-O [78], and HfNbTaTiZr [79].

2.8 Microstructural features in bio-HEAs/CCAs

HEAs/CCAs exhibit a diverse range of microstructures, including phase constitution, grain morphology, precipitate distribution, and structural inhomogeneity at the atomic scale [80-81]. Estimating the phase composition in HEAs, whether solid solution, amorphous, or intermetallic, is often challenging and requires specific consideration of their chemical composition [45]. Numerous studies have observed that the phases in HEAs commonly include random solid solution phases (e.g., BCC, FCC, and HCP), ordered solid solution phases (e.g., B2 and $L1_2$), and intermetallic or complex ordered phases (e.g., σ phase, μ phase, and Laves phase) [45]. This section aims to provide a structured overview of the research advancements in the microstructural characterization of the bio-CCAs.

2.8.1 As-cast microstructure

HEAs produced using the casting method typically show a dendritic microstructure in their as-cast state. Cantor et al. first used equal proportions of 16 and 20 elements and found that the total number of phases was significantly lower than the maximum number allowed by the Gibbs phase rule for equilibrium conditions and even lower than the maximum allowed under non-equilibrium solidification conditions [43]. Furthermore, in addition to the alloy composition, the cooling rate during solidification also plays a crucial role in determining the morphology of the alloys. Senkov et al. were the first to introduce refractory high-entropy alloys (RHEAs), specifically the equiatomic MoNbTaW and MoNbTaVW alloys [82–83]. They reported that both alloys exhibit a single-phase BCC structure with a dendritic morphology when synthesized using the arc-melting method. Other RHEAs, such as TaNbHfZrTi [84], CrNbTiVZr [85], TiZrHfNbCr [86], HfTiVNbTaZr [87], TiMoNbTaWCr [69], MoNbTaWX (X = Cr, Hf, Zr, and Ti) [88], and $Ti_{45}Zr_{37}Nb_{1}6Fe_{1}Mo_{1}$ [89], also show a single-phase BCC structure with characteristic dendritic or interdendritic morphologies.

Todai et al. developed the first biocompatible HEAs using refractory elements in a vacuum arc melting furnace and reported that the quaternary TiNbTaZr alloy exhibits a single-phase BCC structure [40]. However, after adding Mo to TiNbTaZr alloy, the structure changed from a single-phase BCC to a dual-phase BCC (BCC1 + BCC2) structure. The morphology of the as-cast TiNbTaZrMo alloy exhibits a typical dendritic structure, where the dendritic regions are enriched with higher-melting elements such as Ta, Mo, and Nb, while the lower-melting elements (Ti and Zr) segregate in the interdendritic region. Wang et al. also reported similar results in the case of TiZrNbTaMo refractory HEA [34].

Akmal et al. investigated the microstructural evolution in $(MoTa)_xNbTiZr$ CCAs with varying mole fractions of Mo and Ta (x = 0, 0.2, 0.4, 0.6, 0.8, and 1.0) [90]. Their study revealed that the alloys exhibit a single-phase BCC structure up to 0.6 mole fraction of Mo and Ta. Beyond this composition, two distinct BCC phases were observed. Also, as the mole fraction of Mo and Ta increased from 0 to 1, the lattice parameter decreased from 3.41 Å to 3.32 Å. A notable trend was observed in the grain size, which decreased with increasing concentrations of Mo and Ta, as illustrated in Figure 2.10. TEM elemental mapping further showed that in the MoTaNbTiZr alloy, the BCC1 phase is enriched with Mo, Ta, and Nb, while the BCC2 phase is enriched with Zr.

Nagase et al. designed two bio-CCAs, $TiZrHfCr_{0.2}Mo$ and $TiZrHfCo_{0.07}Cr_{0.07}Mo$, and synthesized them using a vacuum arc melting furnace [68]. They reported that both alloys predominantly consist of a BCC solid solution phase, accompanied by a minor Laves phase. The morphology of the alloys consists of a dendritic structure, with the Laves phase distributed in the interdendritic regions. Similarly, the as-cast structure of the TiNbTaZrMoHfWCr bio-super HEA primarily exhibits a major BCC solid solution phase, with a minor C15-type Laves phase [91]. Wang et al. reported that as the amount of Fe in $TiZrHfNbFe_x$ increases from 0 to 2 molar ratio, the structure of the alloy changes from a single-phase BCC structure to a predominant Laves phase with a minor BCC solid solution phase [67].

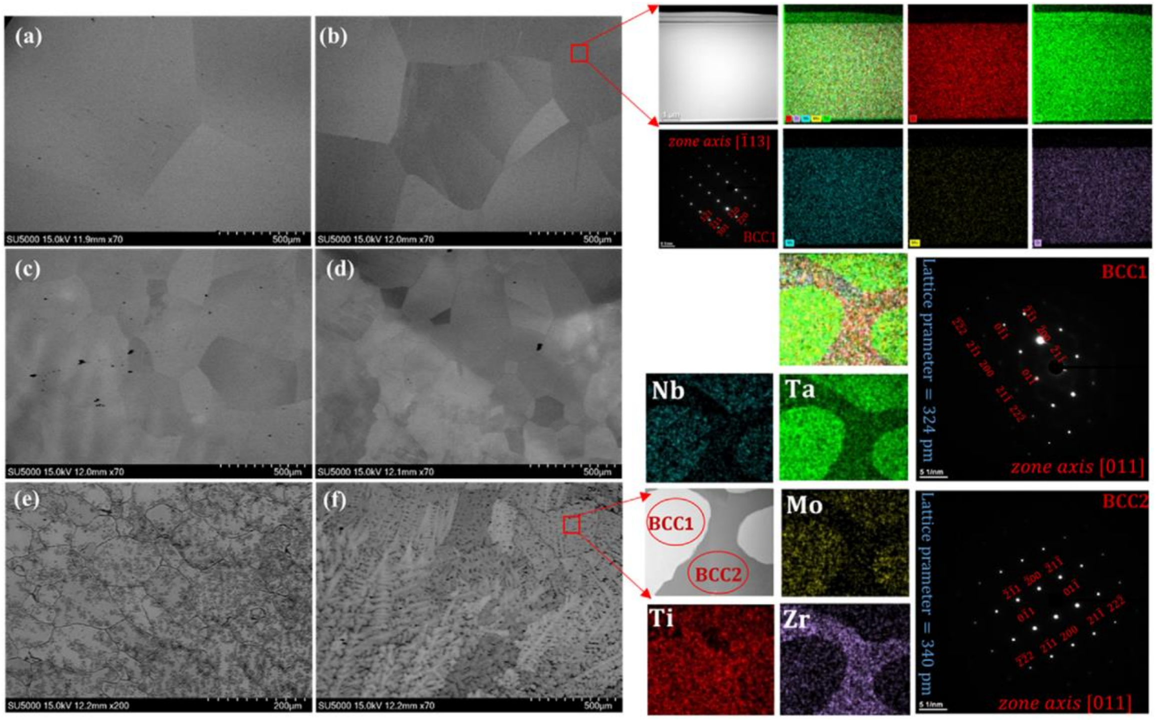

Figure 2.10 SEM-BSE images of the alloys: (a) NbTiZr, (b) $(MoTa)_{0.2}$NbTiZr, (c) $(MoTa)_{0.4}$NbTiZr, (d) $(MoTa)_{0.6}$NbTiZr, (e) $(MoTa)_{0.8}$NbTiZr, and (f) MoNbTaTiZr. TEM-SAED patterns and corresponding elemental mapping for $(MoTa)_{0.2}$NbTiZr and MoNbTaTiZr [90].

2.8.2 Annealed microstructure

Annealing treatment transforms the dendritic morphology observed in the as-cast state into a more or less globular morphology in HEAs [92]. This transformation may occur to reduce the surface area and, consequently, minimize the total surface energy of the system. As a result, coarse dendrites are changed into a nearly globular morphology. Additionally, annealing reduces elemental segregation and promotes a more homogeneous distribution of the constituent elements. Todai et al. also reported similar results, showing that annealing a biocompatible TiNbTaZrMo HEA enhanced the homogeneous distribution of its constituent elements [40].

2.8.3 HPT deformed microstructure

The microstructure developed after HPT deformation exhibits a significant reduction in grain size, ranging from hundreds of microns to tens of nanometers. Notably, the dislocation density increases dramatically, reaching an exceptionally high value of approximately 10^{16} m^{-2} [93-95]. Gubicza et al. reported that for a $Hf_{25}Nb_{25}Ti_{25}Zr_{25}$ CCA, as the number of HPT turns increases from ¼ to 20, the grain size decreases from 105 nm to 28 nm, while the dislocation density increases from 1.38×10^{16} to 2.14×10^{16} m^{-2} [93].

Edalati et al. investigated the effect of HPT on the microstructural evolution of the biocompatible TiAlFeCoNi HEA [75]. They reported that after HPT processing, the ordered $L2_1$ phase disappeared, as indicated by the absence of peaks at 26.37° and 30.54°. This suggests a transformation to the disordered BCC phase, as shown in Figure 2.11 (a). Additionally, the HPT process caused XRD peak broadening, which suggests a decrease in crystallite size, the creation of dislocations, and an increase in lattice strain within the alloy. Similarly, Masis et al. also reported that after HPT processing, crystallite size decreases and dislocation density increases in the case of TiNbZrTaHf HEA, as indicated by peak broadening in the XRD pattern [96].

Figure 2.11 (b-g) shows the EBSD and TEM analysis of a TiAlFeCoNi HEA. The microstructure of the alloy clearly demonstrates that after HPT, a significant refinement of grains occurred, accompanied by the development of numerous dislocations within the material. Stepanov et al. also reported that the as-cast microstructure of a $AlNbTiVZr_{0.5}$ CCA consists of an ordered B2 phase and a C14-type Laves phase [94]. However, as the number of HPT turns increases, the long-range ordering and the amount of the Laves phase decrease. Consequently, after five turns, the microstructure of the alloy changes to a disordered BCC phase, with a small amount of the Laves phase observed.

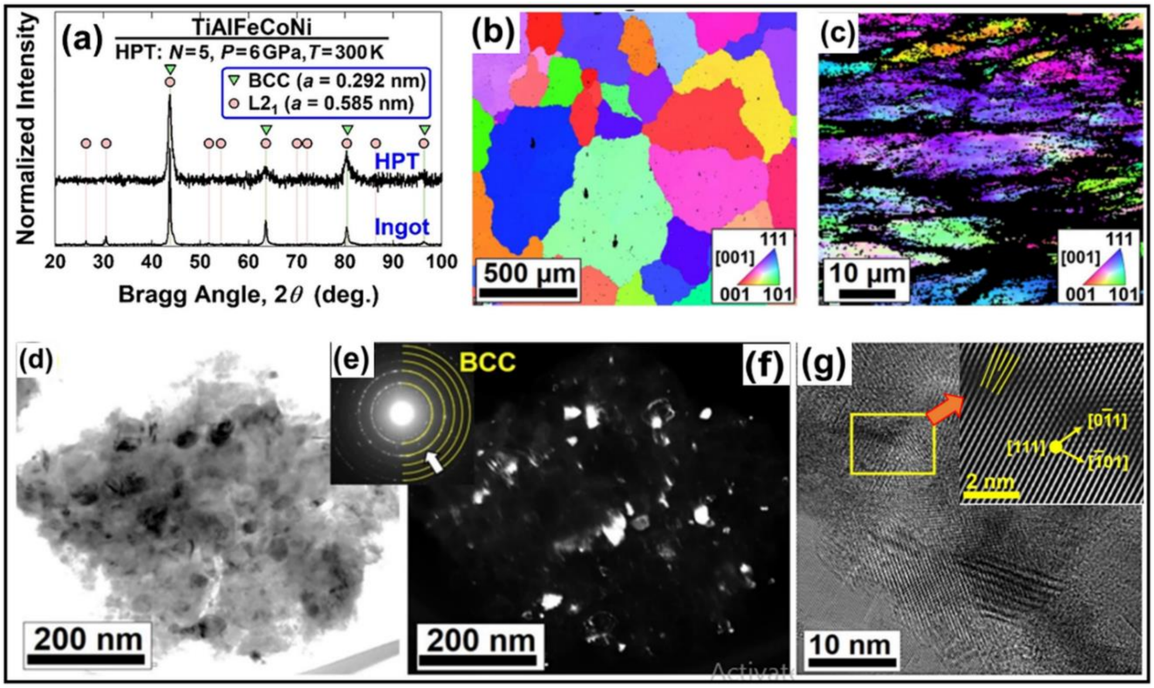

Figure 2.11 Comprehensive analysis of a biocompatible TiAlFeCoNi HEA, includes: (a) XRD pattern, EBSD orientation maps of (b) as-cast and (c) HPT deformed HEA, (d-f) TEM bright-field, dark-field and corresponding SAED pattern of HPT processed, and (g) high-resolution TEM images and lattice images refined by inverse FFT of square regions [75].

2.9 Mechanical properties of bio-HEAs/CCAs

HEAs exhibit superior mechanical properties compared to conventional metallic implants, mainly due to the severe lattice distortion effect [97]. The key mechanical properties, such as strength, hardness, elastic modulus, and fatigue resistance, must be carefully considered when developing bio-CCAs. These mechanical characteristics are closely related to the alloys' microstructures. Notably, HEAs possess diverse and complex microstructures, which can vary significantly, even among alloys with the same elemental composition but different ratios [98]. The processing technique such as heat treatment and other processing methods further influence their structural characteristics; as a result, the mechanical properties are also affected. This section mainly focuses on the mechanical properties of the as-cast, annealed, and HPT-deformed HEAs/CCAs, which are considered blueprints, while considering these novel alloys for biomedical applications.

2.9.1 Hardness and elastic modulus

The hardness and elastic modulus of the alloys mainly depend on their microstructure and processing conditions. In addition to this, the elastic modulus is also influenced by the chemical bond, crystal structure, and chemical composition [97]. As discussed earlier, the elastic modulus is a key property for the stress shielding effect in biomaterials. Several techniques, such as ultrasonic technique and nano/micro-indentation technique can be used to measure these properties. However, nano/micro-indentation is the simplest and commonly used method for evaluating the indentation hardness and elastic modulus of materials that uses the Oliver-Pharr method [34,99].

Wang et al. reported that the hardness of the dendritic and interdendritic regions in a biocompatible TiZrNbTaMo HEA is 6.4 GPa and 5.7 GPa, respectively [34]. These values exceed those predicted by the rule of mixtures, suggesting the contribution of solid-solution strengthening arising from elemental interactions. Similarly, the elastic modulus values of the dendritic and interdendritic regions of this alloy are 161 GPa and 133 GPa, respectively. The higher values observed in the dendritic region may be attributed to the segregation of harder and stiffer elements within the dendritic region compared to the interdendritic region. Gurel et al. reported that the hardness and elastic modulus of BCC-structured biocompatible

TiTaHfNb, TiTaHfNbZr, and TiTaHfMoZr HEAs are 3.5 GPa and 112.2 GPa, 6.5 GPa and 131.6 GPa, and 6.6 GPa and 158.9 GPa, respectively [100].

Edalati et al. reported that the hardness of a HPT-deformed TiAlFeCoNi HEA significantly increases from 8.3 GPa to 11.7 GPa as the number of HPT turns increases from 0 to 5 [75]. However, the elastic modulus of this alloy decreases from 254 GPa to 123 GPa with an increase in the number of turns. This reduction in elastic modulus may be attributed to the significant induction of lattice defects, such as dislocations and vacancies, caused by HPT deformation. Following a similar trend, Stepanov et al. reported that the hardness of the B2 phase in a HPT-processed $AlNbTiVZr_{0.5}$ HEA increased from 573 HV to 713 HV, while the elastic modulus decreased from 128.5 GPa to 106.7 GPa after five HPT turns [94]. Other than HPT, researchers have also explored another method to reduce the elastic modulus by using the super-elastic properties of materials associated with martensitic phase transformation [101-102].

2.9.2 Tensile and compressive properties

Tension and compression tests are among the most fundamental parameters for evaluating the mechanical properties of materials, providing valuable performance data such as yield strength and elongation through stress-strain diagrams. The tensile and compressive properties of bio-CCAs are affected by a complex interaction of various factors, including composition, microstructure, processing techniques, and testing conditions. Gurel et al. reported that after the addition of Zr in TiTaHfNb bio-CCA, the compressive strength of the alloys enhanced almost twice without losing a significant amount of plasticity [100]. Wang et al. also reported that the compressive yield strength and percentage elongation of the vacuum arc melted TiZrNbTaMo HEA are 1390 ± 75 MPa and approximately 6%, respectively [41].

Hua et al. observed that as the Ti content in $Ti_xZrNbTaMo$ (x = 0.5, 1, 1.5, and 2) CCAs increases, the yield strength decreases from 1580 MPa to 1440 MPa. However, the percentage elongation initially decreases from 30% for $Ti_{0.5}ZrNbTaMo$ to 14% for TiZrNbTaMo, and then increases again to 30% for $Ti_2ZrNbTaMo$ CCA. The reduction in strength with increasing Ti content may be attributed to a decrease in the amount of Ta and Mo in the main dendritic region as the Ti concentration increases. This leads to a reduction in modulus mismatch, thereby diminishing solid solution strengthening. Todai et al. reported that the strength in tensile deformation of TiNbTaZrMo bio-HEA improves after annealing treatment. This enhancement can be attributed to grain coarsening and the redistribution of constituent elements [40].

Cizek et al. studied the effect of HPT on the tensile deformation of a HfNbTaTiZr bio-HEA and reported that five rotations of HPT increased the alloy's yield strength from 1030 MPa in the as-cast state to 1480 MPa, with a slight reduction in ductility [79]. This enhancement can be attributed to the significant reduction in grain size caused by HPT, which results in grain boundary strengthening and, consequently, an overall increase in the alloy's strength.

Table 2.2 Mechanical properties of the bio-HEAs/CCAs at room temperature. AC and CR represent the as-cast and cold roll, respectively.

Composition	Processing methods	Phase	Yield strength (MPa)	Ultimate tensile	Percentage	Elastic modul	Ref.

				strength (MPa)	**elongation**	**us (GPa)**	
TiNbWMo	AC	BCC	1058 (C)	-	2.1	-	[83]
TiZrNbTaMo	AC	BCC1 + BCC2	1390 (C)	1390	6	153	[41]
TiNbTaZrMo	AC + Annealing at 1000˚C	BCC1 + BCC2	1150 (C)	-	8	-	[40]
TiZrNbHfTa	AC	BCC	830 (T)	-	9.2	112	[42, 103]
TiZrNbHfTa	AC + CR + Annealing at various temperature (1200˚C – 1350˚C)	BCC (d = 38 µm)	958 (T)	974	20	81	[104]
		BCC (d = 81 µm)	944 (T)	959	18	81	[104]
		BCC (d = 128 µm)	940 (T)	953	15	81	[104]
TiZrNbHfTa	AC + HPT	BCC	1900 (T)	-	7.9	-	[103]
TiNbMoTaW	AC	BCC	1455 (C)	1910	11.5	-	[105]

$Ti_{40}Zr_{20}Hf_{10}Nb_{20}Ta_{10}$	AC	BCC	872.5 (T)	888	23.5	85	[106]
TiMoNbTaW	AC	BCC	1352 (C)	1500	8	137	[69]
TiMoNbTaWCr	AC	BCC	1988 (C)	2250	5.5	170	[69]
$TiZrHfNbFe_{0.25}$	AC	BCC + Laves phase	1100 (C)	1440	20	-	[67]
$TiZrHfNbFe_{0.5}$	AC	BCC + Laves phase	1450 (C)	1450	8	-	[67]
$TiZrHfNbFe_{1.5}$	AC	BCC + Laves phase	1250 (C)	1250	<2	-	[67]
$HfNb_{0.2}Ta_{0.2}TiZr$	AC	BCC + HCP	620 (T)	983	31.8	-	[107]

Bio-HEAs/CCAs presented in Table 2.2 exhibit outstanding mechanical properties, such as high strength and ductility at room temperature. This remarkable combination of properties is achieved through various strengthening mechanisms, including solid solution strengthening ($\Delta\sigma_{ss}$), dislocation strengthening ($\Delta\sigma_{\rho}$), grain boundary strengthening ($\Delta\sigma_{gb}$), and precipitation hardening ($\Delta\sigma_{ppt}$). Consequently, the yield strength (σ_y) of the HEAs is the sum of the lattice friction stress (σ_{fr}) and the contributions from all the strengthening mechanisms, which can be represented by the following equation [108]:

$$\sigma_{\mathrm{y}} = \sigma_{\mathrm{fr}} + \Delta\sigma_{\mathrm{ss}} + \Delta\sigma_{\rho} + \Delta\sigma_{gb} + \Delta\sigma_{ppt} \ \ldots\ldots\ldots\ldots (2.7)$$

2.10 Tribological behavior of bio-HEAs/CCAs

Wear is a common type of mechanical failure that leads to alterations in the shape, size, positional accuracy, and surface characteristics of components [24]. In the human body, micro-movements at the bone-implant interface are inevitable, making implant wear and tear a persistent concern regardless of the material used. Additionally, implant wear releases cytotoxic metal ions into the body, leading to implant loosening, as schematically illustrated in Figure 2.12 [25,109]. Aseptic loosening, caused by osteolysis, is the primary reason for implant failure and accounts for over 75% of total joint replacement failures [110]. Therefore, the wear resistance of implants is a critical factor in determining the long-term clinical success of metallic biomaterials. The corrosive nature of the body's physiological environment enhances wear, significantly shortening the lifespan of implant materials [111]. Table 2.3 provides an overview of the findings from recent studies on the friction and wear characteristics of bio-HEAs/CCAs.

Wear rate measures the amount of material, either by mass or thickness, removed from a surface over a specific period. It can be measured in different ways, with the simplest method involving the comparison of wear resistance between samples by assessing weight loss. The wear resistance of the alloys is related to the hardness of the alloy [59]. In the case of metallic alloys, higher the strength and hardness, higher the wear resistance. Wang et al. reported that with an increase in the Fe content of $\mathrm{TiZrHfNbFe_x}$ CCA, the volume fraction of the Laves phase accordingly increases. This structural evolution leads to a notable increase in hardness, which, in turn, enhances the wear resistance of the alloy [67].

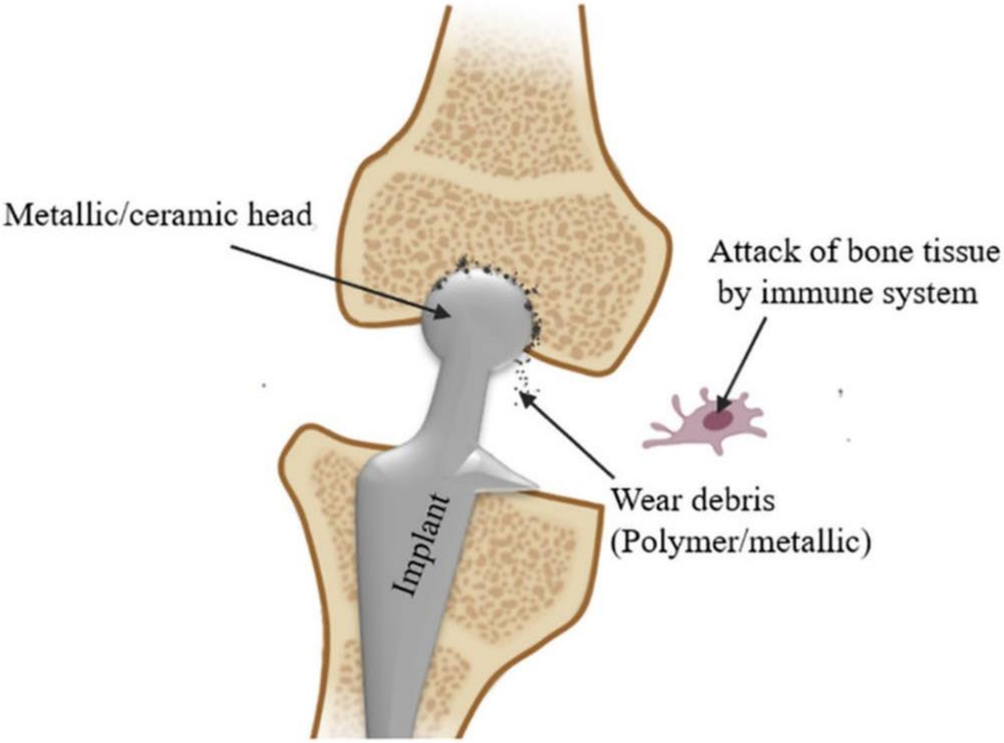

Figure 2.12 Schematic diagram of implant wear [25].

Table 2.3 Friction and wear behavior of bio-HEAs/CCAs.

HEAs/CCAs	Phase	Test conditions	Research finding	Ref.
TiZrMoNbTa	BCC	Applied load 5,10,15 N, wet condition	The alloy demonstrated a low wear rate and friction coefficient, along with rapid and stable passivation in SBF solution, achieving four times greater wear resistance than stainless steel.	[112]

$(TiZrNbTa)_{90}Mo_{10}$	BCC	Applied load varies from 2-20 N, dry condition	The wear mechanism changes based on the amount of the applied load, with abrasive wear being predominant at low loads and three-body abrasive wear taking over at higher loads.	[111]
$Ti_xZrNbTaMo$	BCC	Applied load 5 N, dry and wet conditions	As the Ti content increases, the wear resistance of HEAs decreases. Further, the wear rate is lower in wet friction conditions than in dry friction conditions.	[113]
$Ti_{42.5}Zr_{42.5}Nb_5Ta_{10}$	BCC	Applied load 5 N, wet condition	The 880ºC annealed alloy exhibited superior wear resistance compared to cp-Ti, Ti6Al4V, and as-cast alloys in SBF solution.	[114]
Ti-12Mo-6Zr-2Fe	BCC	Applied load 5 N, dry and wet conditions	Hydroxyapatite can naturally form on alloy surfaces when immersed in an SBF solution. The primary wear mechanisms	[115]

			include abrasive wear and tribo-chemical interactions.	
TiMoNbTaW and TiMoNbTaWCr	BCC	Applied load 5 N, wet conditions	Both HEAs exhibit superior wet-wear resistance compared to CoCrMo alloys. Also, with Cr addition in TiMoNbTaW RHEA, a ten-fold enhancement in wear resistance was observed. The worn surface exhibited a smooth wear scar without noticeable plastic deformation. The reduction of sliding-induced abrasion led to a considerable decrease in the friction coefficient.	[69]
$TiZrHfNbFe_x$	BCC + Laves Phase	Applied load 5 N, dry and wet conditions	Under dry friction conditions, the wear resistance of Ti-Zr-Hf-Nb-Fe HEAs improves as the Fe content increases, due to enhanced hardness. While corrosive wear is observed when these HEAs slide in a	[67]

			PBS solution, their wet-wear resistance surpasses that of the Ti6Al4V alloy.	

2.11 Corrosion resistance

The corrosion of implant materials poses a global challenge to patient health and safety. This degradation process can release toxic substances, leading to inflammatory reactions, infections, and various complications. Consequently, it drives up health-care costs and often necessitates revision surgeries or implant replacements, further exposing patients to additional risks [60,116]. Once orthopedic implants are placed in the human body, they are subjected to a consistent temperature of 37°C within an electrolyte environment. This environment contains organic acids, alkali and alkaline earth metal ions (such as Na^+, K^+, and Ca^{2+}), and Cl^- ions, along with proteins, enzymes, and cells. These factors can contribute to the corrosion of the metal components [117].

Most bio-HEAs/CCAs contain passivating elements such as Ti, Zr, and Mo, which facilitate the formation of a protective passivation layer. The specific role of each element on the alloy's structure and the composition of the passive film can vary, influencing the electrochemical behaviour based on the alloy's type and composition [118]. As a result, HEAs generally exhibit superior corrosion resistance compared to conventional alloys. To evaluate the corrosion resistance of bio-CCAs, various simulated physiological environments can be utilized, including simulated body fluid (SBF), phosphate buffer solution (PBS), fetal bovine serum (FBS), Ringer's solution, Hank's solution, NaCl solution, simulated blood, and artificial saliva (AS) [25].

Potentiodynamic polarization experiments are commonly used to determine electrochemical parameters such as corrosion potential (E_{corr}) and corrosion current density (I_{corr}), which are then analyzed to evaluate the corrosion resistance of alloys [119]. Generally, a higher E_{corr} and a lower I_{corr} indicate better corrosion resistance, as corrosion resistance is directly proportional to E_{corr} and inversely proportional to I_{corr}. [120]. Yang et al. reported that TiZrHfNbTa HEA exhibits a lower corrosion current density compared to Ti6Al4V alloy, indicating superior corrosion resistance [121]. Wang et al. replaced Ta with Fe in the aforementioned alloy to develop a new $TiZrHfNbFe_x$ HEA and investigated the influence of Fe on its corrosion behavior. Their findings revealed that the corrosion current density initially decreased and then increased as the Fe content increased, as shown in Figure 2.13 (a). The $Fe_{0.5}$ alloy exhibited the lowest corrosion current density, signifying the highest corrosion resistance. Also, no corrosion pits were observed on the $Fe_{0.5}$ alloy sample surface after the corrosion test [67].

Figure 2.13 (b) shows the X-ray photoelectron spectroscopy (XPS) analysis of the surface film on the corroded surface of $TiZrHfNbFe_x$ HEA. The analysis indicates that the surface film is composed of TiO_2, ZrO_2, HfO_2, Nb_2O_5, and Fe_2O_3. Among these, the $Fe_{0.5}$ alloy exhibits a higher concentration of O^{2-} and Nb^{5+}, which contributes to its superior corrosion resistance.

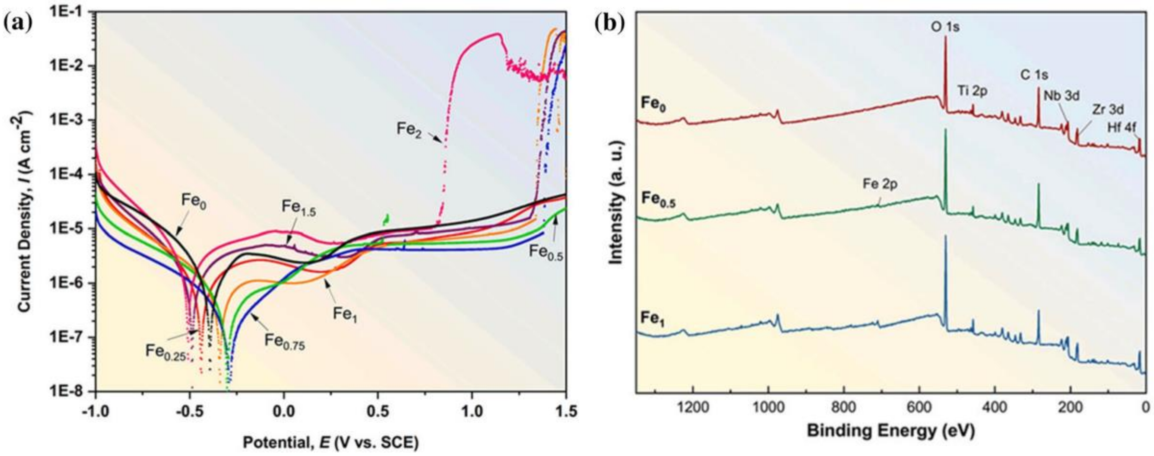

Figure 2.13 (a) Potentiodynamic–polarization curves of the Ti-Zr-Hf-Nb-Fe$_x$ (x=0, 0.25, 0.5, 0.75, 1, 1.5, and 2) HEAs in the PBS solution and (b) XPS full spectrum on the corroded surfaces of the Ti-Zr-Hf-Nb-Fe HEAs [67].

Chavan et al. reported that, after the addition of Cr to TiMoNbTaW HEA, the potentiodynamic polarization curve shifted left and upward, as shown in Figure 2.14 (a) [69]. This indicates that the addition of Cr increases the E_{corr} and decreases the I_{corr}, leading to an improvement in the alloy's corrosion resistance. The Nyquist and Bode plots confirm that the passive film formed on the surface of the Cr-containing HEA is stronger compared to the HEA without Cr. Figure 2.14 (e, f) shows the corroded surface morphology of both HEAs: the HEA without Cr exhibits numerous corrosion pits, whereas no pits are observed in the Cr-containing HEA. This confirms that the addition of Cr significantly enhances the corrosion resistance of the TiMoNbTaW HEA. Table 2.4 exhibits the electrochemical parameters of the various bio-HEAs/CCAs in physiological solutions.

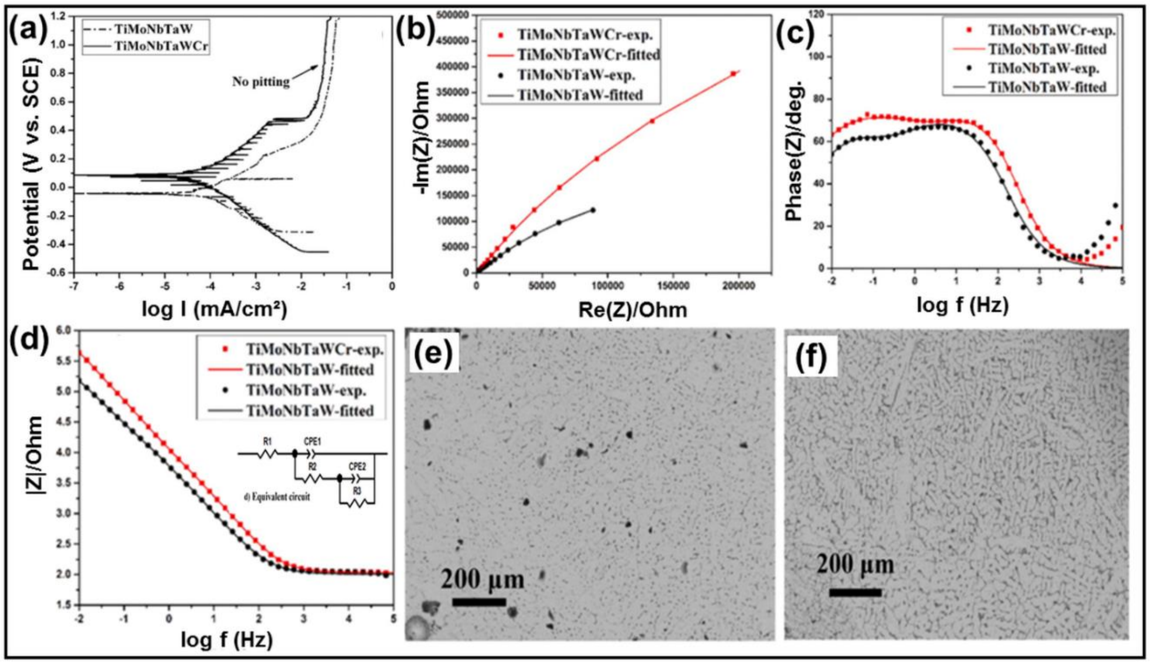

Figure 2.14 Electrochemical measurement of TiMoNbTaW and TiMoNbTaWCr HEAs in Hank's solution (a) potentiodynamic polarization curve, (b) Nyquist plot, (c, d) Bode phase angle and impedance modulus plots, and (e and f) corroded surface morphology of without Cr and with Cr, respectively [69].

Table 2.4 Electrochemical parameters of the various bio-HEAs/CCAs in physiological solutions.

Alloys	Solution	E_{corr}	I_{corr}	Ref.
TiZrHfNbTa	Hank's solution	- 395 mV	8.0×10^{-3} A·m^{-2}	[121]
$Ti_{20}Zr_{20}Hf_{20}Nb_{20}Ta_{20}$	Hank's solution	- 302 mV	0.08×10^{-3} A·m^{-2}	[122]
$(Ti_{0.2}Zr_{0.2}Hf_{0.2}Nb_{0.2}Ta_{0.2})_{97}Sn_3$	Hank's solution	- 456 mV	0.21 10^{-3} A·m^{-2}	[123]
Ti-25Nb-10Ta-1Zr-0.2Fe	Ringer's solution	- 71.7 mV	2.20×10^{-7} A·cm^{-2}	[124]
TiZrNbHfSi	Ringer's solution	- 330 mV	8.0×10^{-8} A·cm^{-2}	[125]
$Ti_{40}Mo_{15}V_{15}Cr_{15}Zr_{15}$	Ringer's solution	- 393 mV	7.12×10^{-7} A·cm^{-2}	[126]
TiZrNbTaMo	PBS	- 607 mV	8.90×10^{-7} A·cm^{-2}	[41]
TiZrHfNbTa	PBS	- 391 mV	7.20×10^{-7} A·cm^{-2}	[42]

$TiZrHfNbFe_{0.25}$	PBS	- 420 mV	9.33×10^{-7} A·cm^{-2}	[67]
$Ti_{1.5}ZrTa_{0.5}Nb_{0.5}W_{0.5}$	PBS	- 160 mV	8.90×10^{-7} A·cm^{-2}	[127]
$(MoTa)_{0.2}NbTiZr$	PBS	- 530 mV	-	[90]
$(TiZr)_{75}Nb_{15}Mo_{10}$	SBF	- 317 mV	74.2×10^{-6} A·cm^{-2}	[128]
$(TiZrNb)_{14}SnMo$	SBF	- 850 mV	2.01×10^{-6} A·cm^{-2}	[129]
Ti-35Nb-2Ta-3Zr	SBF	- 339 mV	2.05×10^{-7} A·cm^{-2}	[130]

2.12 In-vitro biocompatibility

Biocompatibility encompasses the intricate biological, physical, and chemical interactions between a material and a living organism. It is the most critical factor in the development and design of biomedical materials. Before being implanted into a biological system, biomaterials must undergo comprehensive biocompatibility assessments, including evaluations of cytotoxicity (to identify and address harmful substances), as well as considerations related to surgical procedures, implant site compatibility, and load-bearing capabilities [131].

Additionally, cytocompatibility encompasses the alloy's ability to support cell adhesion and its cytotoxicity [61]. Cell adhesion is essential for maintaining the stability of tissue structures and serves as a regulator of cell motility and function, thereby playing a significant role in cell proliferation and differentiation [132]. Meanwhile, cytotoxicity serves as a key indicator for assessing the biological activity of cells on the alloy surface, making it a crucial parameter for the in-vitro evaluation of bio-CCAs. Commonly used cell lines in these studies include human aortic smooth muscle cells, osteoblasts, human osteosarcoma cells, human epithelial fibroblasts, L929 mouse fibroblast cells, and mouse embryo osteoblast precursor cells [133].

At present, cytotoxicity tests for bio-HEAs involve in-vitro cell culture, where cell survival rates and cell adhesion on the alloy surface are evaluated to determine their biological properties. Todai et al. conducted a cell culture experiment using human osteoblasts and reported that cell adhesion on the surface of TiNbTaZrMo bio-HEA is higher compared to cp-Ti and 316L SS, as shown in Figure 2.15 (a-d) [40]. Additionally, cell adhesion increased after annealing treatment. This improvement may be attributed to the more homogeneous distribution of the constituent elements after annealing. Further, quantitative analysis confirmed that the annealed HEA exhibits superior biocompatibility (higher cell density on alloy surface) compared to as-cast HEA, cp-Ti, and 316L SS, as shown in Figure 2.15 (e).

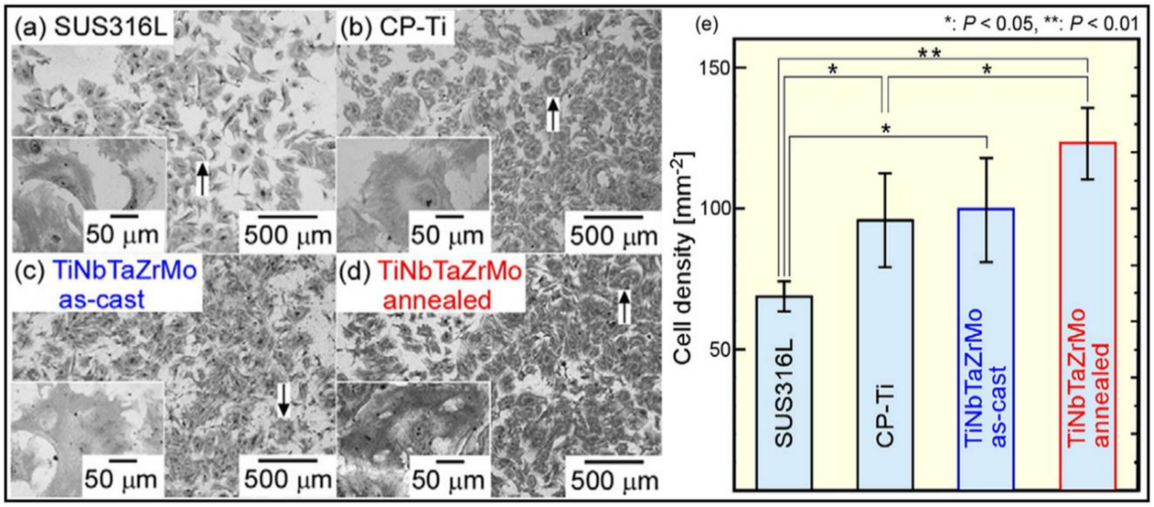

Figure 2.15 Giemsa staining of the osteoblasts cultured for 24 h on (a) 316L SS, (b) cp-Ti, (c) as-cast TiNbTaZrMo, (d) annealed TiNbTaZrMo HEA, and (e) quantitative analysis of cell density after 24 h cultivation on each alloy [40].

Newell et al. reported that the live (green) cells on the surface of Co-Cr-Fe-Ni-based CCAs are higher compared to those on SS, Ni, and untreated (control) surfaces, as shown in

Figure 2.16 (a-f) [134]. However, both Ni and SS exhibit a higher number of dead (red) cells compared to CCAs, which may be attributed to the release of toxic elements in physiological environments. This suggests that CCAs possess higher biocompatibility than Ni and SS after 168 hours of incubation. Quantitative analysis further confirms that the viability of the Ni sample decreases significantly at 96 and 168 hours, potentially due to the release of Ni ions. These ions demonstrate cytotoxic properties, leading to a substantial reduction in cell numbers, as illustrated in Figure 2.16 (g).

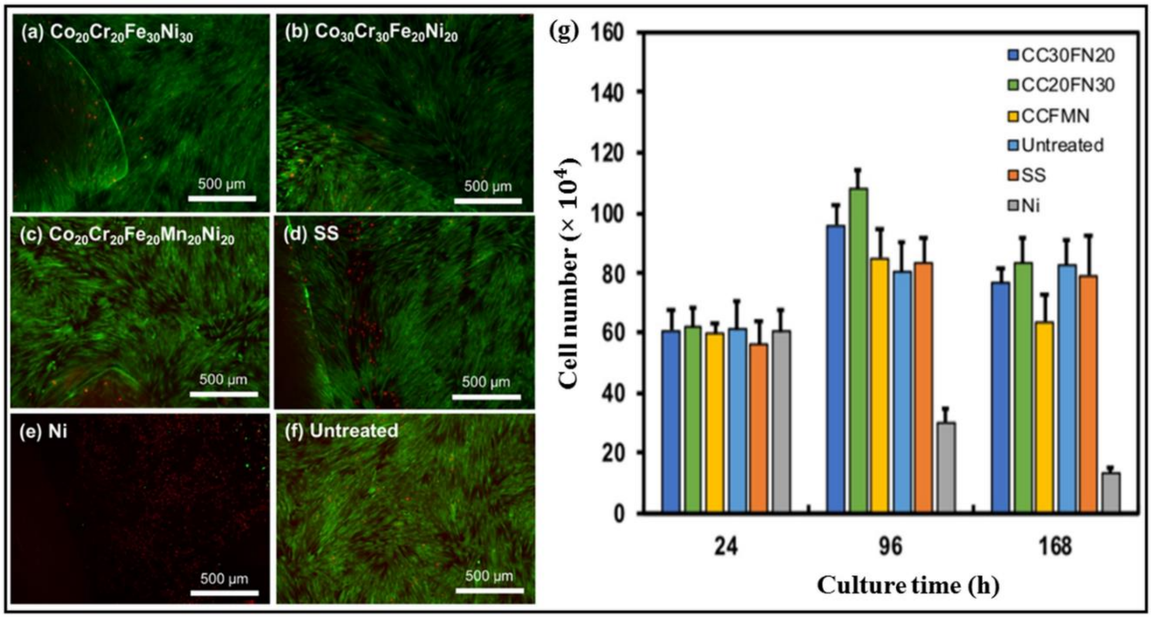

Figure 2.16 Live/dead imaging after 168 h incubation of (a) $Co_{20}Cr_{20}Fe_{30}Ni_{30}$ (CC20FN30), (b) $Co_{30}Cr_{30}Fe_{20}Ni_{20}$ (CC30FN20), (c) $Co_{20}Cr_{20}Fe_{20}Mn_{20}Ni$ (CCFMN), (d) stainless steel (SS), (e) Ni, and (f) untreated wells, with live (green) and dead (red) cells, and (g) cell number as a function of time [134].

Wang et al. investigated the adhesion of human fibroblasts to equiatomic TiZrHf and quinary $Ti_{40}Zr_{20}Hf_{10}Nb_{20}Ta_{10}$ CCAs [106]. The cells on the $Ti_{40}Zr_{20}Hf_{10}Nb_{20}Ta_{10}$ alloy were observed to be flatter and more widely spread. These findings indicate that the $Ti_{40}Zr_{20}Hf_{10}Nb_{20}Ta_{10}$ alloy exhibited much higher biocompatibility than cp-Ti, whereas

TiZrHf showed only a slight improvement in biocompatibility over cp-Ti. Yang et al. reported that equiatomic TiZrHfNbTa HEA demonstrates superior cell adhesion, viability, and proliferation behavior compared to Ti6Al4V alloy in MC3T3-E1 pre-osteoblast cells [121]. The MoNbTaTiZr HEA exhibited excellent in-vitro biocompatibility with stem cells and osteoblast cells [112]. The presence of multiple filopodia extensions and polygonal cell morphology in osteoblasts further confirmed strong cell adhesion, robust growth, and active proliferation.

Chavan et al. reported that Cr plays an important role in the biocompatibility of TiMoNbTaW HEA when tested with MC3T3-E1 pre-osteoblast cells [69]. They demonstrated that after the addition of Cr to TiMoNbTaW HEA, cell adhesion, proliferation, and viability significantly increased, indicating that Cr enhanced the biocompatibility of the CrTiMoNbTaW alloy. Nagase et al. also reported that the biocompatibility of alloys depends on their compositions [68]. Figure 2.17 (a-d) illustrates that the morphology of cells on both CCAs, $TiZrHfCr_{0.2}Mo$, and $TiZrHfCo_{0.07}Cr_{0.07}Mo$, is almost identical, but the cell density differs. The cell density of the Co-containing HEA is lower compared to the Co-free alloy, such as $TiZrHfCr_{0.2}Mo$, due to the cytotoxic response of cobalt in the cell culture medium. However, the cell densities of both CCAs are higher compared to 316L SS and CoCrMo alloys, as shown in Figure 2.17 (e).

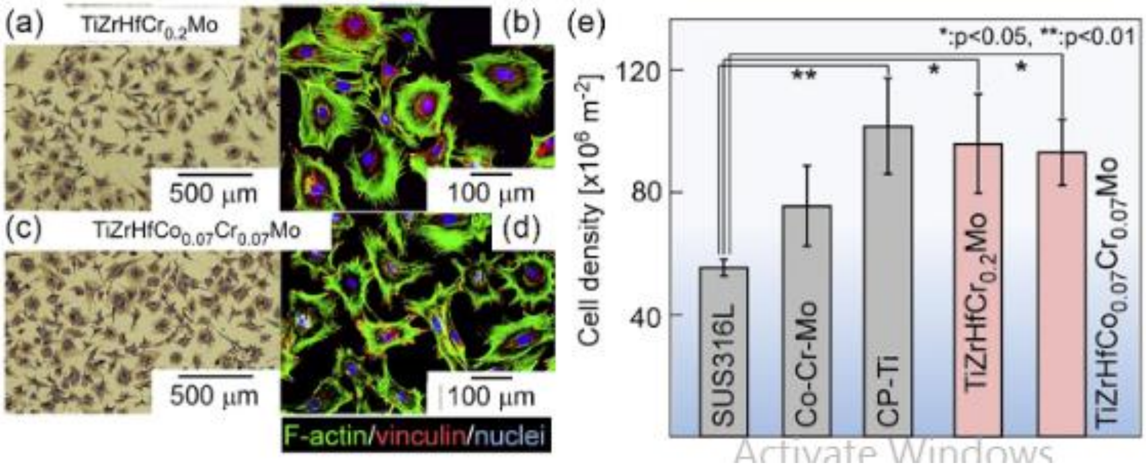

Figure 2.17 Giemsa staining images of osteoblasts cultured on fabricated specimens: a) TiZrHfCr$_{0.2}$Mo and c) TiZrHfCo$_{0.07}$Cr$_{0.07}$Mo HEAs. Fluorescent images of osteoblast adhesion on fabricated specimens: b) TiZrHfCr$_{0.2}$Mo and d) TiZrHfCo$_{0.07}$Cr$_{0.07}$Mo HEAs. e) Quantitative analysis of cell density on the specimens [68].

2.12.1 Factors affecting cell adhesion

Cell adhesion to metallic alloy surfaces is affected by a combination of the alloy's surface characteristics, the physiological environment, and the inherent properties of the cells. These factors play a crucial role in areas such as biomaterials, tissue engineering, and implant design, as they govern the biocompatibility and functionality of metallic implants. The main parameters are:

2.12.1.1 Chemical composition

The chemical composition of an alloy can significantly influence cell adhesion due to its effects on surface properties, corrosion resistance, and the biological environment's interaction with the material. Many alloys form oxide layers (e.g., Ti alloys develop a titanium dioxide layer) that influence surface chemistry and wettability [135]. These oxide layers can either promote or inhibit protein adsorption, which is critical for cell adhesion and viability. Cemin et al. reported that the presence of oxide on the surface of the alloy significantly enhanced the cell adhesion of a NbTaTiVZr(O) alloy [136]. Additionally, alloys containing specific elements (such as Ni, Al, V, or Co) may release ions that are potentially harmful to cells or change local pH levels, thereby reducing cell viability and proliferation. On the other hand, bioactive ions like Ti, Nb, Zr, and Mo can enhance cell adhesion and proliferation. The composition of an alloy, along with its processing, influences its grain size and structure. Smaller grains increase surface energy, which can improve protein adsorption and support cell adhesion [96,137].

2.12.1.2 Surface Roughness and Topography

Surface roughness is one of the main factors influencing cell adhesion behavior [138-139]. Quite a few investigations have shown that surface roughness can impact cell adhesion regardless of the cell type or matrix material [140]. In addition, based on surface irregularities, roughness is categorized into macroscopic, microscopic, submicron, and nanometer scales. Various levels of surface roughness have distinct impacts on cells. Macroscopic roughness has minimal influence on cell adhesion, as the large irregularities provide ample space for cells to spread and grow. In contrast, micron and submicron roughness exhibit dual but generally positive effects on cell adhesion and growth. Nano-roughness, however, closely mimics the morphology of natural tissue and significantly promotes cell adhesion, growth, and maturation. For example, increasing the nanometer-scale roughness of the biomaterial surface enhances adhesion and growth [140].

2.12.1.3 Surface Energy

Surface free energy is a thermodynamic parameter that plays a crucial role in the study of interfacial phenomena. It has a significant impact on cell adhesion, as any change in its value modifies surface wettability, thereby influencing cell behavior [141]. The cell-biomaterial interaction is determined by the physicochemical properties of the biomaterial, with alterations in the surface's chemical composition affecting its surface free energy.

Additionally, surface free energy is an intrinsic characteristic of solid materials and cannot be directly measured. However, it can be calculated using contact angle measurements. The surface free energy or adhesion work (W_{adh}) can be determined using the following equation [142]:

$$W_{adh} = \gamma \times (1 + \cos\theta) \text{ ………………… (1.8)}$$

where, γ denotes surface tension, and θ represents the contact angle. Surfaces with higher surface free energy can enhance the production of pro-angiogenic growth factors and support the differentiation of human aortic endothelial cells. This indicates that such surfaces may enhance the biocompatibility of implant materials by promoting vascularization and improving tissue integration. The surface free energy also affects bacterial adhesion, with higher values generally leading to reduced bacterial attachment [143].

2.12.1.4 Surface wettability

The wettability of surfaces, characterized by their hydrophobicity or hydrophilicity, can significantly influence protein adsorption and subsequent cell attachment [135,144]. Previous studies suggest that cells are more likely to adhere to hydrophilic surfaces ($\theta < 90°$). This is because surface wettability affects the type, structure, and binding strength of proteins adsorbed from the culture medium, which in turn influences cell attachment. On hydrophobic surfaces ($\theta > 90°$), extracellular matrix (ECM) proteins such as fibronectin (FN), vitronectin, and collagen are adsorbed in a denatured form, making them unsuitable for cell binding. However, excessively hydrophilic surfaces ($\theta < 5°$) can also prevent the binding of cell adhesion components, thereby hindering cell attachment [141]. In contrast, cells adhere and proliferate more effectively on biomaterial surfaces with moderate hydrophilicity ($40° < \theta < 70°$) [142,145-147].

2.13. Scope of the present thesis

The literature review indicates that very few investigations have reported the development of bio-CCAs using a combination of refractory and non-refractory elements. However, these studies do not provide comprehensive information on all the properties required for biomedical applications. Additionally, no literature is available that seeks to unravel the underlying mechanisms of biocompatibility by studying the effect of crystallographic texture on the biocompatibility of these CCA systems. The present thesis addresses some of these gaps with the objective of developing a novel CCA system comprising refractory and non-refractory elements. It systematically investigates all the properties necessary for biomedical applications. However, this chapter provides the foundational background for the study, and the subsequent results chapters of the thesis broadly focus on the following objectives:

[1]. To develop a Ti-Nb-Mo-Fe-Cr-based CCA and investigate its microstructure, mechanical properties, and corrosion behaviour.

[2]. To study the microstructure, mechanical, and tribological properties of a Ti-Zr-Nb-Mo-Fe-Cr based bio-CCA.

[3]. To evaluate the corrosion and cytocompatibility behaviour of a Ti-Zr-Nb-Mo-Fe-Cr based bio-CCA.

[4]. To study the crystallographic texture dependence of biocompatibility of the Ti-Zr-Nb-Mo-Fe-Cr based bio-CCA.

[5]. To evaluate the role of high pressure torsion on microstructure and properties of the Ti-Zr-Nb-Mo-Fe-Cr based bio-CCA.